

JGR Atmospheres

RESEARCH ARTICLE

10.1029/2018JD029834

Key Points:

- The diurnal cycles of summer precipitation, including the prominent peak shortly after midnight, are reproduced well by 4-km forecasts
- The diurnal variations of the southerly low-level jet are found to play dominant roles in controlling the precipitation diurnal cycles
- The diurnal variations of low-level jet can be explained well by the boundary layer inertial oscillations theory of Blackadar

Correspondence to:

M. Xue,
mxue@ou.edu

Citation:

Zhang, Y., Xue, M., Zhu, K., & Zhou, B. (2019). What is the main cause of diurnal variation and nocturnal peak of summer precipitation in Sichuan Basin, China? The key role of boundary layer low-level jet inertial oscillations. *Journal of Geophysical Research: Atmospheres*, 124, 2643–2664. <https://doi.org/10.1029/2018JD029834>

Received 15 OCT 2018

Accepted 3 FEB 2019

Accepted article online 7 FEB 2019

Published online 14 MAR 2019

What Is the Main Cause of Diurnal Variation and Nocturnal Peak of Summer Precipitation in Sichuan Basin, China? The Key Role of Boundary Layer Low-Level Jet Inertial Oscillations

Yuehan Zhang¹, Ming Xue^{1,2} , Kefeng Zhu¹ , and Bowen Zhou¹ 

¹Key Laboratory of Mesoscale Severe Weather/Ministry of Education and School of Atmospheric Sciences, Nanjing University, Nanjing, China, ²Center for Analysis and Prediction of Storms and School of Meteorology, University of Oklahoma, Norman, OK, USA

Abstract The precipitation in Sichuan Basin (SB), China, exhibits pronounced diurnal variation, including minimum rainfall in daytime and a prominent peak near midnight. This study investigates the primary mechanism of precipitation diurnal variation in SB using forecasts from three summer months of 2013 produced at a 4-km grid spacing. The model forecasts reproduce the observed spatial distributions and diurnal cycles well, including the peak precipitation in SB at around 02 local solar time (LST). Contrary to the common belief that emphasizes the solenoidal effects associated with the Tibetan and Yunnan-Guizhou Plateaus, prominent diurnal inertial oscillations of boundary layer south-southwesterly low-level jet into SB are shown to play more important roles in modulating the diurnal cycles of precipitation in SB. A basinwide moisture budget analysis is performed to reveal that the moisture flux from the southeast side of the basin dominates within the diurnal oscillations of the net moisture flux into the basin, and the much enhanced nocturnal low-level jet plays a crucial role in the formation of nocturnal precipitation within the basin. The net moisture flux into SB reaches maximum at around 22 LST, the time boundary layer perturbation winds from the daily mean in the direction normal to the southeastern boundary of SB reach maximum, which is about 4 hr before precipitation peak at around 02 LST. Shallow thermally forced nighttime downslope flows and daytime upslope flows on the Tibetan Plateau and Yunnan-Guizhou Plateau slopes contribute only a small portion of moisture fluxes through the basin boundaries.

1. Introduction

Sichuan Basin (SB) is located immediately east of the Tibetan Plateau (TP) in southwestern China (Figure 1). It is one of the warm season precipitation maximum centers in China (J. Lin & Yang, 2014; Yu et al., 2009; Zheng et al., 2016). Heavy rainfall can cause river, urban and rural area flooding, mountain flash floods and landslides, and interrupt transportations, farming, and industrial activities and lead to great economic losses (D.-Q. Huang et al., 2015). According to the China Meteorological Administration's yearbook of meteorological disasters, the environmental and social costs of floods were as high as 48.24 billion RMB (about \$7.26 billion) in Sichuan Province in 2013 summer.

Studies have shown that precipitation in SB has strong diurnal variations. Nocturnal precipitation has been found to account for up to 70% of the total precipitation in SB (Zheng et al., 2016), which is usually called “Bashan Yeyu” (nocturnal precipitation in Bashan Mountains; Lv, 1942). Both rain gauge and satellite observations reveal that, from pre-Meiyu season to midsummer, precipitation peak usually occurs at night and early morning in SB (Bao et al., 2011; G. Chen et al., 2013; Qian et al., 2015; Shen & Zhang, 2011; Xu & Zipser, 2011; Yin et al., 2009; Yu, Xu, et al., 2007; Yu, Zhou, et al., 2007; Yuan et al., 2012). Within the basin, there are also diurnal changes in the precipitation distribution. Convection tends to first appear on the eastern slope of the TP around noon, and propagates eastward into the basin by late evening (Jin et al., 2012). After midnight and through the early morning hours, the precipitation area tends to cover the entire SB (Qian et al., 2015).

Precipitations over China have been studied extensively using numerical simulations (Shen & Zhang, 2011; Yuan, 2013). Most studies, however, focus on the precipitation in central eastern China (G. Chen et al., 2009,

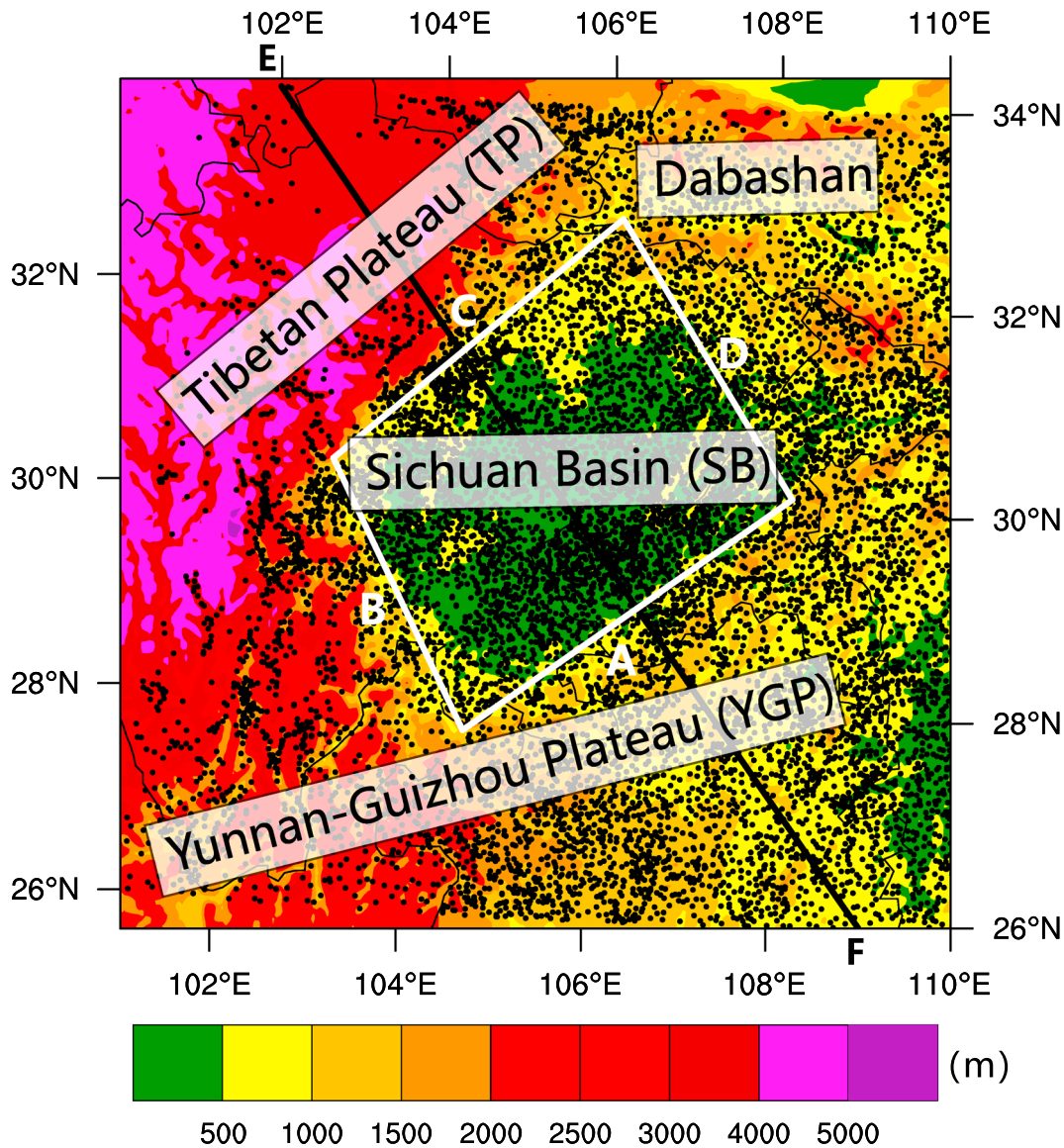


Figure 1. The terrain height (shaded) in and around the Sichuan Basin, China, together with surface precipitation observation stations (black dots) used to verify precipitation forecasts. Thin black lines are province boundaries. Tibet Plateau (TP), Sichuan Basin (SB), Yunnan-Guizhou Plateau (YGP), and Dabashan Mountains are marked in the picture. The white box ABCD encloses the control volume for budget analysis in this paper. Line EF indicates the location of the cross section shown in Figure 4.

2010; H. L. Huang et al., 2010; Shen & Zhang, 2011; Xu & Zipser, 2011; Yuan, 2013), while only a few studies focus on SB precipitation (Jin et al., 2012; Qian et al., 2015). Often, large discrepancies exist between the simulated and observed precipitation in SB, including their spatial pattern, intensity, and timing (Zhou et al., 2008). For instance, using the RegCM3 model at a resolution of 60 km, Shen and Zhang (2011) reproduced the nocturnal precipitation peak in SB but the simulated peak time was 2 hr earlier than observed and daytime precipitation was overestimated. Partly for such reasons, and the fact that high-frequency, high spatial resolution precipitation data have not been generally available until more recently, there have been few in-depth studies on the exact mechanisms of precipitation diurnal variations, in particular, the nocturnal peak in SB.

The common belief attributes the daytime minimum and nighttime maximum of precipitation in SB to thermally driven vertical circulations due to heating and cooling of elevated surrounding plateaus, that is, the TP to the west northwest and the Yunnan-Guizhou Plateau (YGP) to the south southwest. Jin et al. (2012) proposed a conceptual model for the development of SB precipitation. According to their conceptual model,

during the day, the TP is a heat source and the upslope winds form on the eastern slope of the TP. The upward motions at the western edge of the basin are apt to produce convective rainfall while the returning circulations and warm advection aloft act to suppress precipitation over the basin during the day. At night, the thermodynamic condition is reversed. The TP becomes colder than the basin, with downslope winds developing on its eastern slope, pooling into the basin, and creating convergence there that promotes nighttime precipitation. Their conceptual model also points out the contribution of nocturnal low-level jet (LLJ) in transporting moist air into the basin, aiding the development of nighttime precipitation. Alternatively, Li et al. (2008) emphasize the negative role of afternoon cloud cover in southwest China that leads to unfavorable conditions for afternoon precipitation. Other studies (H. Chen et al., 2010; Yu, Zhou, et al., 2007) alluded to the possible role of cloud top radiative cooling in enhancing nighttime rainfall (X. Lin et al., 2000; Steiner et al., 1995). As alluded to earlier, another possible contributor to nighttime precipitation in the basin is the eastward movement into the basin of convective systems that developed over the TP in the afternoon (Jin et al., 2012; Qian et al., 2015). Hu et al. (2016) and Mai et al. (2019) found, however, that only a small percentage of Tibetan convective systems moved eastward out of the Plateau in the climatological studies. Furthermore, many such convective systems first undergo weakening at the edge of the Plateau before increasing in intensity again over the plains to the east. The relative contributions by such migrating convective systems to nighttime precipitation within SB remains unclear.

Over the Great Plains of the United States, nocturnal LLJ has been realized to be an important cause for nighttime rainfall (Bonner, 1966; Higgins et al., 1997; Trier et al., 2014; Wallace, 1975), due to enhanced moisture transport and low-level convergence created by the LLJ at its northern terminus. As discussed in Xue et al. (2018), the formation mechanisms of the Great Plains nocturnal LLJ include the initial oscillation theory of Blackadar (1957) related to the diurnal change in the effect of surface friction on the boundary layer flow and the thermal wind adjustment theory of Holton (1967), which explains the diurnal change in wind in terms of the horizontal pressure gradient force changes due to the heating and cooling of sloping terrains. Based on the Blackadar theory, ageostrophic wind vector rotates clockwise with time at a period of $2\pi/f$ with f being the Coriolis parameter (Blackadar, 1957; Markowski & Richardson, 2010), while diurnal change in the background geostrophic wind is ignored in the model. In general, the Blackadar inertial oscillation theory explains better the behaviors of the Great Plains LLJ than the Holton theory, although most recently a unified theory has been proposed that combines the two effects (Shapiro et al., 2016), resulting in a better fit of the theoretical prediction to observations. In reality, both processes may have contributions.

Anomalous low-level winds and their links to nighttime precipitation peak have been recognized in a number of climatological studies of precipitation over central and eastern China (e.g., H. Chen et al., 2010; Du & Rotunno, 2014) although the main cause of the anomalous winds tends to remain unexplained. Most recently, Xue et al. (2018) demonstrated that enhanced low-level moisture flux convergence into the Meiyu frontal zone by LLJ associated with boundary layer inertial oscillations of southerly monsoon flows is the primary cause of nearly morning rainfall peak in Meiyu season over central and eastern China. The characteristics of LLJs over mostly eastern China have been studied in recent studies of Du et al. (2012) and Du et al. (2014), but these studies do not address the relationship between LLJ and precipitation diurnal cycles. The characteristics and variability of the LLJ over the YGP within a case was studied in He et al. (2016), but again, the relationship between the LLJ and diurnal cycle of rainfall was not investigated. The main mechanism of the diurnal cycle of SB precipitation is still unclear.

Recently, Zhu et al. (2018) presented evaluations of precipitation forecasts over China in summer months of 2013 and 2014, as produced by the Advanced Research Weather Research and Forecast (WRF-ARW) model (Skamarock et al., 2005) at Nanjing University (WRF_NJU hereafter) at a horizontal grid spacing of 4 km. Compared with operational global models, WRF_NJU better captures precipitation over China in terms of spatial distribution, intensity, and diurnal variations, including over SB. In this study, the WRF_NJU forecasts in June-July-August of 2013 are used to study the primary mechanism of precipitation diurnal variations, in particular, of the precipitation peak near midnight in SB.

Specifically, we will perform a quantitative analysis of low-level moisture fluxes passing through four side boundaries of a control volume occupying SB, and try to understand the relative contributions of upslope/downslope circulations along the plateau slopes, and flows from the southside and eastside that strengthen at night in the form of nocturnal LLJ, in forcing/controlling precipitation within SB. Further,

the reasons for the diurnal changes of the LLJ are also discussed. Different from the conventional wisdom and earlier study of Jin et al. (2012) that emphasize the direct thermal effects of the orography and the associated circulations.

The rest of the paper is organized as follows. The precipitation observations and the forecast data set used in this study are described in section 2. Section 3 compares spatial distribution and diurnal variation of precipitation in the forecast data set with observations. Quantitative analyses of low-level moisture fluxes into SB are performed in section 4, together with discussions on the mechanisms of precipitation diurnal cycle. Summary and conclusions are given in section 5.

2. Observations and Forecast Configuration

The precipitation observation data are obtained from the China Meteorological Administration with more than 30,000 sites across China and most of them are automated weather stations (Luo et al., 2013). The data have been used to evaluate precipitation forecasts of WRF_NJU over summer months of 2013 and 2014 in Zhu et al. (2018). Simple quality control procedures were applied, including removal of duplicate sites, time, and space continuity check, and exclusion of abnormal values, as was described in Zhu et al. (2018). The stations are shown as black dots in Figure 1 within our study domain. The white box shown in Figure 1 is the region for our low-level moisture flux budget analysis to be discussed later.

The model data set is from real-time forecasts produced at Nanjing University using the Advanced Research Weather Research and Forecast (WRF-ARW) model (Skamarock et al., 2005), which covers the entire mainland China. The model was run at a 4-km grid spacing during June through August since 2013 at Nanjing University, China, and the forecasts are produced twice daily, starting from NCEP Global Forecasting System 00 and 12 UTC analyses, and forced at the lateral boundaries by Global Forecasting System real-time forecasts at 3-hourly intervals. Zhu et al. (2018) show that the forecasts capture well the precipitation diurnal cycles in 2013 and 2014 when verified over entire domain, as well as the spatial distributions and season variations of precipitation, better than operational global forecasts from several numerical weather prediction centers. The heavy precipitation center near SB is also captured well. The same forecast data set was used in Xue et al. (2018) to investigate the diurnal cycle mechanism of Meiyu front precipitation.

The WRF_NJU model domain has $1,409 \times 1,081$ horizontal grid points and 50 vertical levels. The physics parameterizations used are the Morrison two-moment microphysics (Morrison et al., 2005; Pleim, 2006), Asymmetrical Convective Model version 2 (ACM2) PBL (Pleim, 2007), Pleim-Xiu land-surface model (Pleim & Xiu, 1995), and the CAM short- and long-wave radiation schemes (Collins, 2004). No cumulus parameterization is used. These options were chosen based on extensive tests in the context of multiphysics ensemble using the same model grid configurations with the 21 July 2012 Beijing extreme rainfall event (Zhu & Xue, 2016). In this paper, we focus on the diurnal variation of precipitation over the SB (Figure 1) in 2013 summer (June to August) in the 12- to 36-hr forecasts initialized at 12 UTC, which is 07 LST at SB.

3. Assessment of the Precipitation Forecasts Over SB

The diurnal variations of mean hourly precipitation within the region enclosed in white box in Figure 1, in both the observations and forecast, are shown in Figure 2. The observed precipitation was first analyzed to the model grid using Cressman interpolation then averaged over all grid points within the white box and over 92 days of June through August 2013. Both observations and WRF forecasts show a clear unimodal structure. A precipitation maximum is found at 02 LST and minimum values are found between 12 and 18 LST (with a slight enhancement at 14 LST), consistent with previous climatological studies (Jin et al., 2012; Yu, Zhou, et al., 2007). Precipitation is very weak throughout the day, from 10 to 19 LST. In the observations, nighttime peak is about 0.47 mm/hr, while daytime minimum is about 0.14 mm/hr, a factor of 3.3 difference. In general, the forecast shows a very good agreement with the observations, except for some underestimation of precipitation intensity. The forecast precipitation is not exactly periodic because of forecast errors (the data are from 12 and 36 hr of forecasts).

Figure 3 shows the average hourly precipitation in SB at 07, 13, 19, and 01 LST in observations and WRF_NJU forecasts. In the early morning (Figures 3a and 3b), heavy precipitation is found mostly in the northwest part of the basin, along its northwest and north rims. There is also some precipitation near the

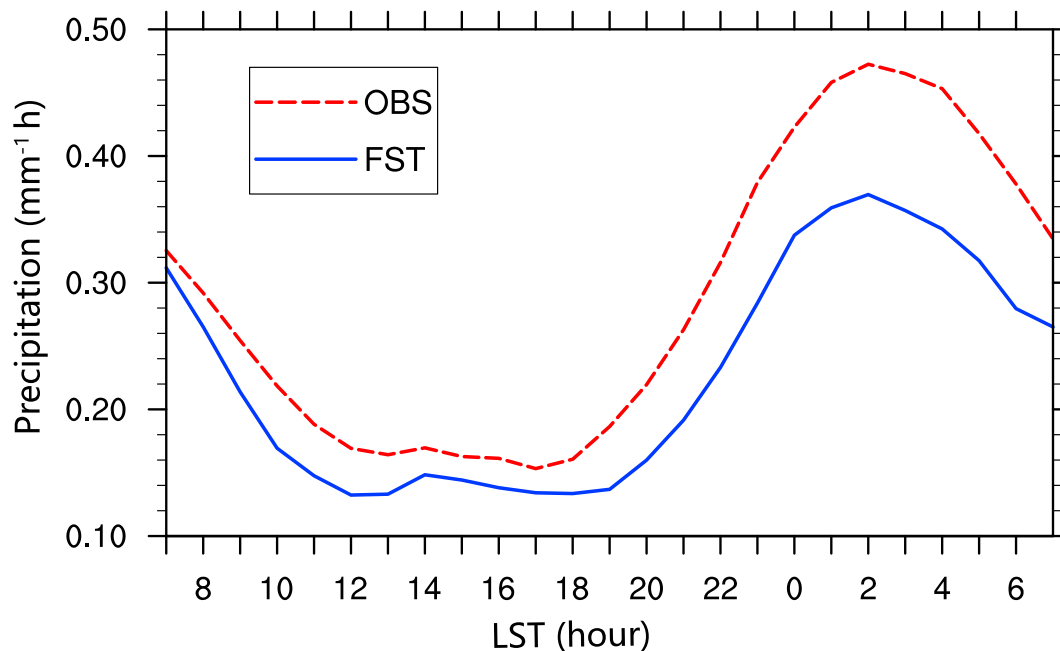


Figure 2. The time series of spatially and temporally averaged hourly rainfall over Sichuan Basin (within the white box in Figure 1) in June–August 2013. The red dashed line indicates the WRF_NJU forecast (FST) and the blue line represents the observation (OBS) results.

basin center. By 13 LST (Figures 3c and 3d), most of the precipitation has dissipated, with the central part of the basin mostly free of precipitation. By 19 LST, significant precipitation has developed along the northwest and southwest rims, mostly along the eastern slope of TP and northern slope of YGP. At 01 LST, the entire basin is filled with precipitation, especially in the observations (Figures 3g and 3h). Much of this precipitation dissipates significantly over the next 6 hr so that only that near the northern rims remains (Figures 3a and 3b). Overall, the model captures the horizontal distribution, intensity, and diurnal cycle of the precipitation quite well, with relatively small quantitative differences, and the amount of precipitation at different times is consistent with the time series of hourly average precipitation shown in Figure 1. For this reason, the model data set can be used to investigate the causes of precipitation diurnal variation, and in particular, the mechanism of the prominent precipitation maximum at night. Such investigation is performed in the next section.

4. Mechanisms of SB Precipitation Diurnal Cycles

4.1. Diurnal Variations of Model-Simulated Circulations

We first examine the model-simulated circulations at different times of the day, averaged over the 92 days. Figure 4 shows the wind vector and vertical velocity fields within a northwest-southeast vertical cross section along line E-F in Figure 1, every 6 hr during a day. The wind vectors are projected into the cross section. At 07 LST, upward motion, though relatively weak compared to that at 01 LST (Figure 4d), is found in almost the entire basin at the lower levels, especially near the TP slope, where precipitation is found in Figure 3a. Weak and shallow downslope flows are found along the eastern slope of TP, clearly due to nighttime cooling (Figure 4a). In the early afternoon at 13 LST, the circulations along the TP slope and within the basin are reversed. Downward motion is found filling the entire basin width, while strong upslope winds appear on the eastern slope of TP (Figure 4b). Associated with the strong upslope flows is a narrow band of downward compensating flow as part of the thermally driven solenoidal circulation, as indicated in Figure 4b. Such circulation patterns correspond to the precipitation minimum in the afternoon (Figures 2 and 3d). At 13 LST, the low-level winds over the ~1-km high plateau to the southeast of SB (which we will call eastern YGP, see Figure 1) are southerly, but relatively weak (Figure 4b).

In 19 LST, most of the domain is still filled with downward motion at the lower levels, although upward motion is found above 2.5 km mountain surface layer (Figure 4c). A very thin layer of downslope flow is

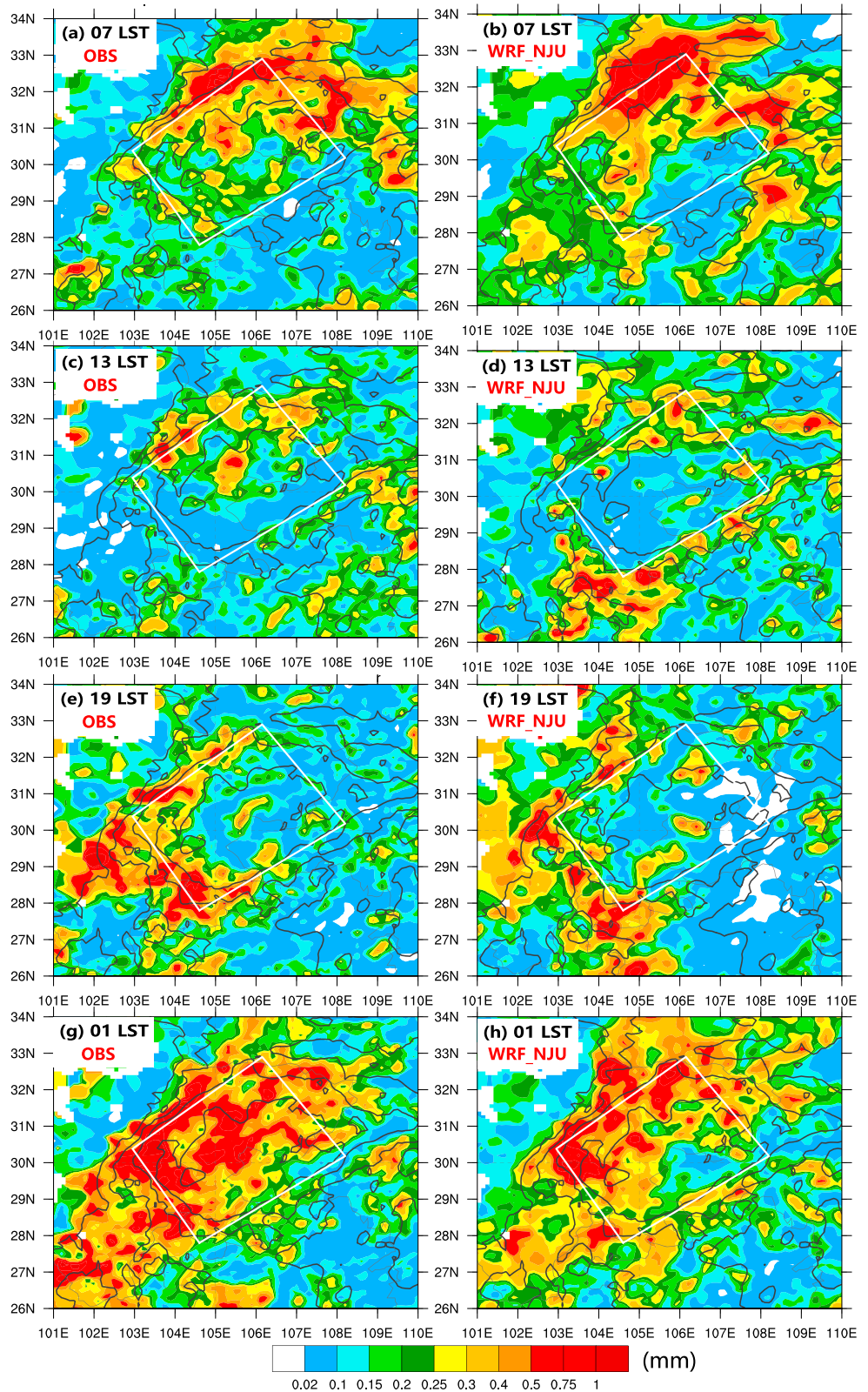


Figure 3. The time series of observations (OBS) from surface rain gauge measurements at left panels (a, c, e, and g) and WRF_NJU-simulated rain at right panels (b, d, f, and h) in 2013 summer (shaded), at 07, 13, 19, 01 LST. The bold black contours denote the terrain. The white box is the focus area, representing the Sichuan Basin. The rain gauge observations are remapped onto the WRF grid using bilinear interpolation method.

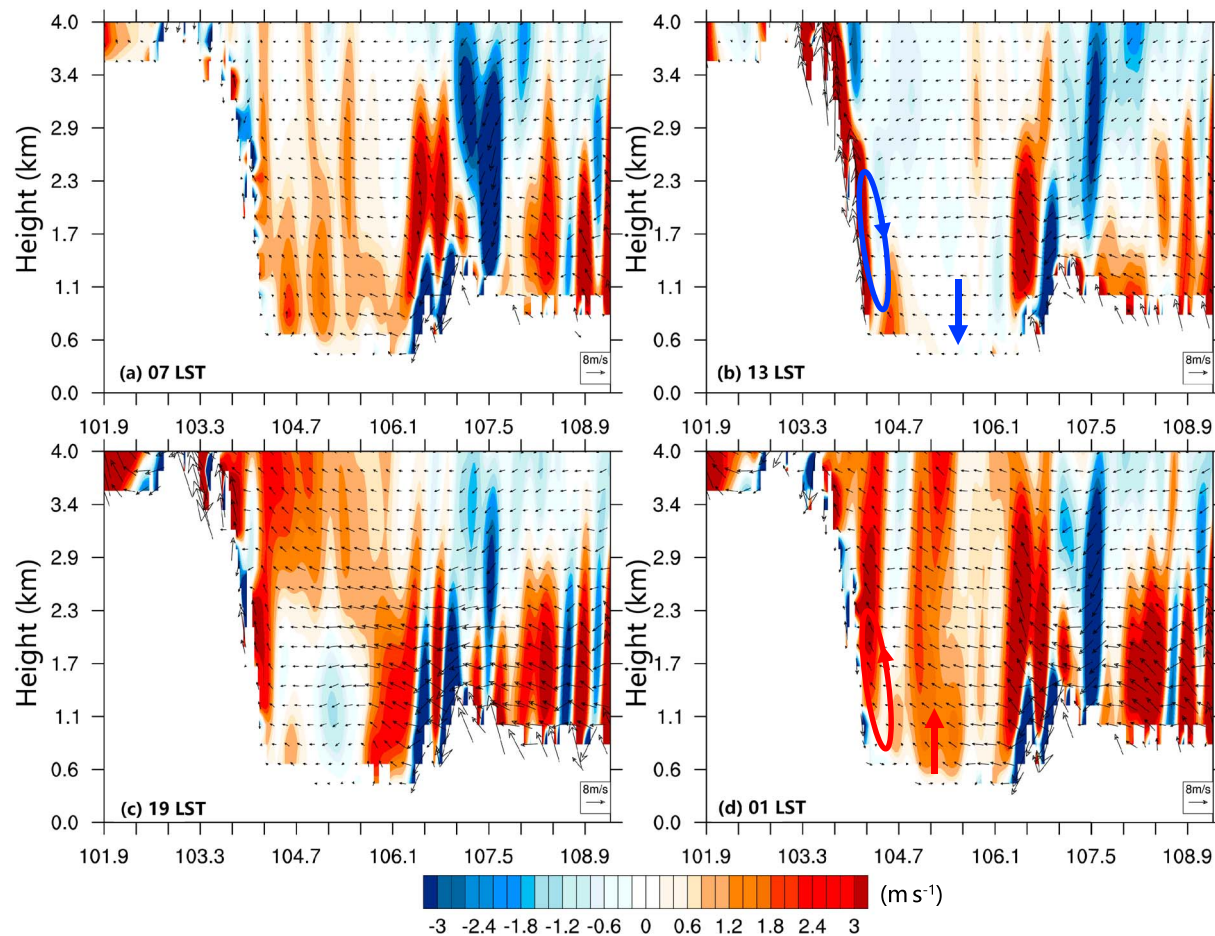


Figure 4. The cross-section EF on Figure 1, the time series of total wind vectors along the cross, the vertical wind speed (shaded), from (a) 07 LST, (b) 13 LST, (c) 19 LST to (d) 01 LST, every 6 hr. Time average is performed over the entire 2013 summer.

starting to appear on the eastern slope of TP. At the same time, the southeasterly winds on eastern YGP to the southeast have strengthened, and upward motions are also found in the area (Figure 4c). At this time, precipitation is still mostly absent within the basin (Figures 2 and 4f). After midnight at 01 LST, the circulation over the slope of TP is reversed from that of 13 LST and a shallow layer of downslope winds has developed along the eastern slope of TP, underneath much stronger upward winds located above and further into the basin. Based on the relative strengths of the downward and upward flows near the slope, such upward winds do not appear to be completely forced by the downslope flows; something else should have contributed toward the forcing of such strong upward motion.

Strong and deep upward motion is also found near the basin center and the southeast rim of the basin, and such upward motion matches the strongest precipitation within the basin at this time (Figure 3h). Over eastern YGP to the southeast, southeasterly winds are now much stronger (Figure 4d). In fact, such strong winds are part of the nocturnal LLJ that peaks at about 500 m above ground level (AGL) in this region (Figure 4d). As we will show later, this LLJ and its diurnal circulation play an important role in modulating the precipitation diurnal cycle within SB.

To see more clearly the near-surface winds, including the upslope and downslope winds on the plateau slopes, horizontal wind fields at 200 m AGL are shown in Figure 5. At 07 LST, southerly winds pooling into the basin from its southeast rim turns toward the southwest near the foot of TP slope, and within the basin contributing to a cyclonic circulation with associated convergence (Figure 5a). Because the mountain is colder at this time, downslope winds are clearly evident on the northern slope of YGP and are also visible along the lower part of the TP slope, consistent with the vertical circulations seen in Figure 4a. By 13 LST,

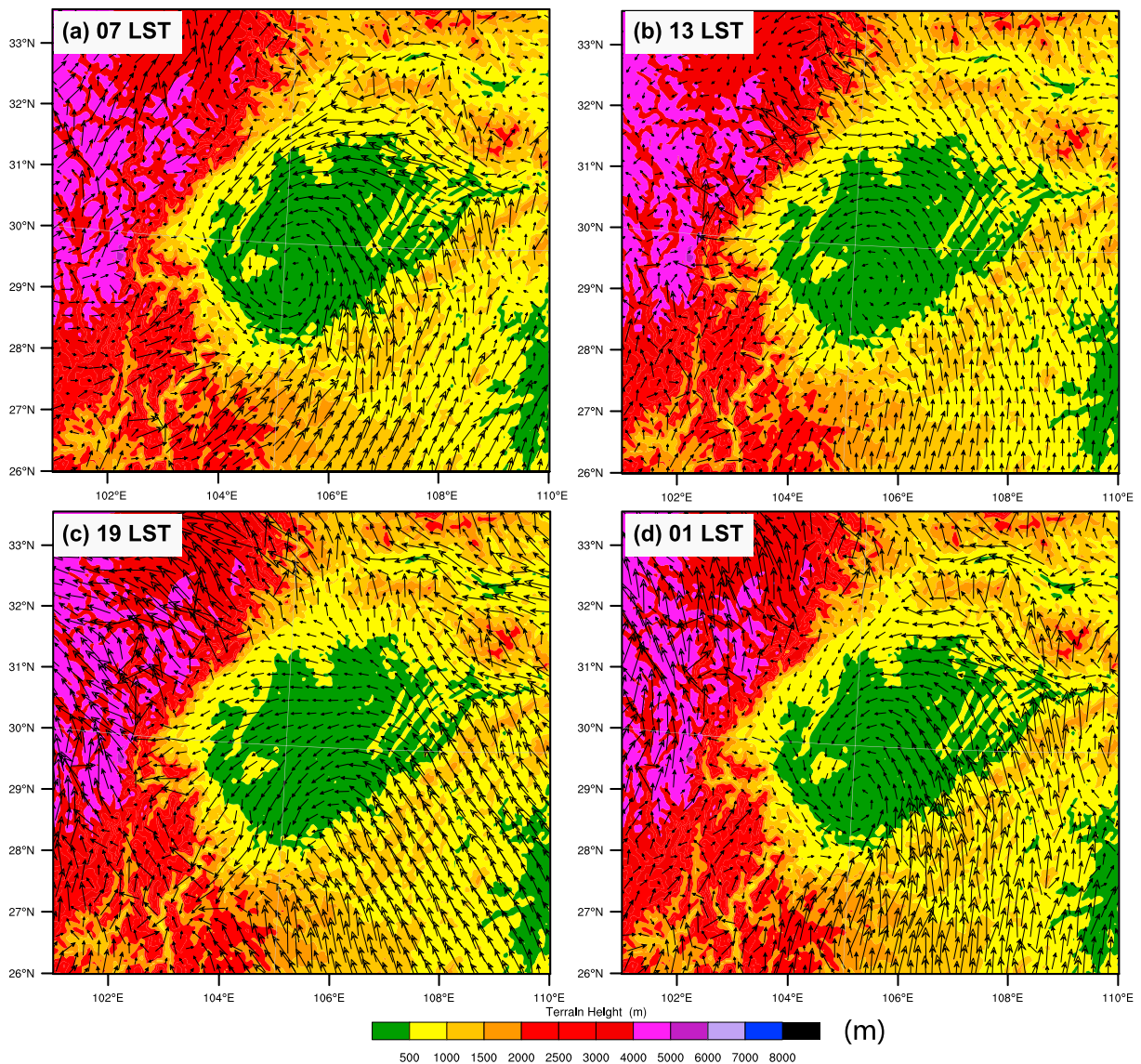


Figure 5. The WRF_NJU-simulated horizontal wind fields at 200 m AGL, at (a) 07, (b) 13, (c) 19, and (d) 01 LST. The shading is for terrain height.

the southeasterly winds down the southwest rim weakens significantly, and upslope winds develop on all three other slopes of SB (Figure 5b), with apparent divergence flow patterns throughout the basin even near the cyclonic circulation center. Such flow patterns are clearly not favorable to precipitation at this time.

In the early evening at 19 LST, the upslope flows on the northern slope of YGP and eastern slope of TP are much stronger (Figure 5c), leading to significant precipitation at those locations (Figures 3e and 3f). Within the basin, however, the flow is strongly divergent, corresponding to still very little precipitation within the basin (Figures 3e, 3f, and 2). At 01 LST, the winds over eastern YGP become much stronger than earlier, as indicated by the sizes of the arrow heads. Near the foot of YGP and TP slopes, the surface flows are generally into the basin, although further up on the TP slope the flows are still upslope. In general, surface convergences within the basin and into the cyclonic circulation center are clearly evident. The much stronger southerly flow into the basin (which peaks at around 22 LST, see Figure 9 later) clearly brings much more moisture into the basin, and also creates extra convergence forcing that promotes precipitation. Not surprisingly, the heaviest precipitation is found near this time in the basin (Figures 3g, 3h, and 5d).

Throughout the day, the variations in the near-surface horizontal winds (Figure 5) are consistent with the diurnal variations of winds in the vertical cross sections (Figure 4). For the flow over eastern YGP to the

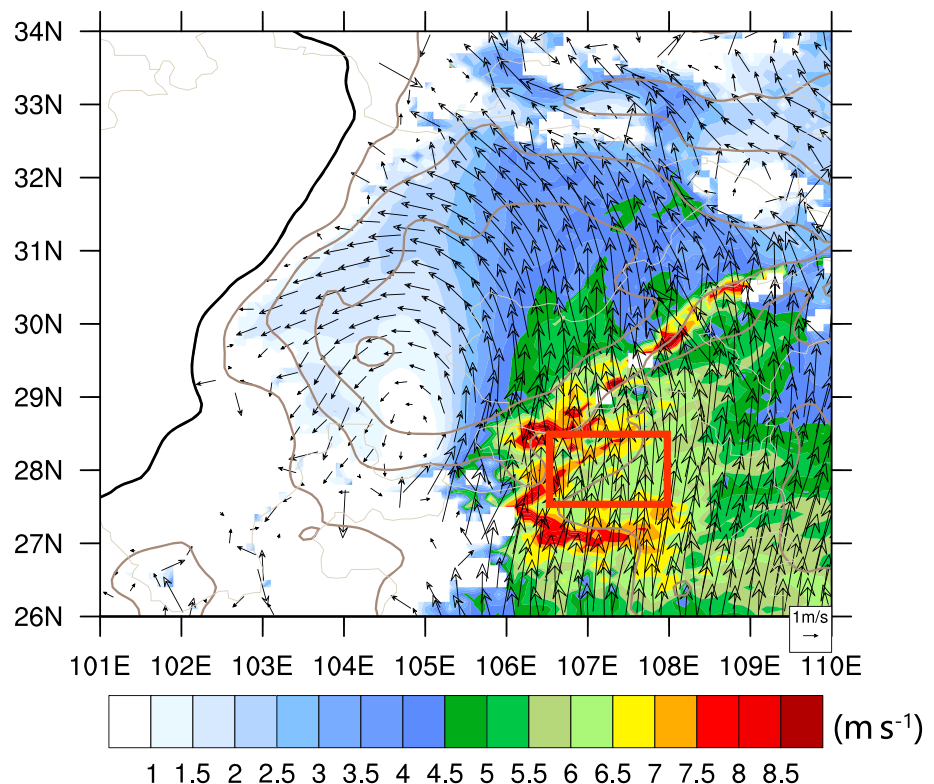


Figure 6. The WRF_NJU-simulated prevailing wind (averaged over all hours of 92 days in 2013 summer) vector and horizontal wind speed (shaded) at 850 hPa. The terrain is superimposed as contours and the black contour represents the TP at 3,000-m height.

southeast of SB, a part of the noted wind speed changes, we also notice wind direction changes among the four times of the day shown in Figure 5. We will examine such changes in more details in the next section.

4.2. The Mechanism of Nocturnal LLJ and its Impact on the Nocturnal Rainfall

To help understand the diurnal variations of the low-level flows over eastern YGP, we show in Figure 6 the daily average wind vectors and wind speed at 850 hPa, which at this location is about 500 m AGL. The winds are obtained by averaging over 24 hr of forecasts (from 12 to 36 hr) over 92 days, and we will refer to them as the prevailing or background winds. The mean prevailing winds over eastern YGP that feed SB are southerly and southwesterly (Figure 6), and they provide the most important moisture supply for precipitation within SB. When the moist air encounters the eastern slope of TP, most of it veers from southerly to easterly and northeasterly, a small part of it climbs the slope (Figure 5).

Given the daily mean winds, deviation or perturbation winds from the mean, defined as $\vec{V}' = \vec{V} - \vec{V}$, at 850 hPa are plotted in Figure 7, together with the deviation wind speed. One aspect that is immediately noticeable is the change in the deviation wind direction over eastern YGP; the deviation wind direction rotates clockwise throughout the day, changing from eastward (Figure 7a), to mostly southward (Figures 7b–7d), to westward (Figure 7e), then northward (Figures 7f and 7h) and eventually back to eastward (Figure 7h) from early morning through noon into night and the morning. Such clockwise rotation of deviation wind vector suggests that inertial oscillation of boundary layer winds as explained by the Blackadar (1957) boundary layer inertial oscillation may be at play here.

Here, we point out that strictly, the Blackadar inertial oscillation theory predicts diurnal changes of ageostrophic wind assuming that the background geostrophic wind does not change. In Xue et al. (2018) that studies the role of boundary layer inertial oscillations on the diurnal cycles of Meiyu frontal precipitation, ageostrophic wind is examined that is calculated as deviation of total wind from

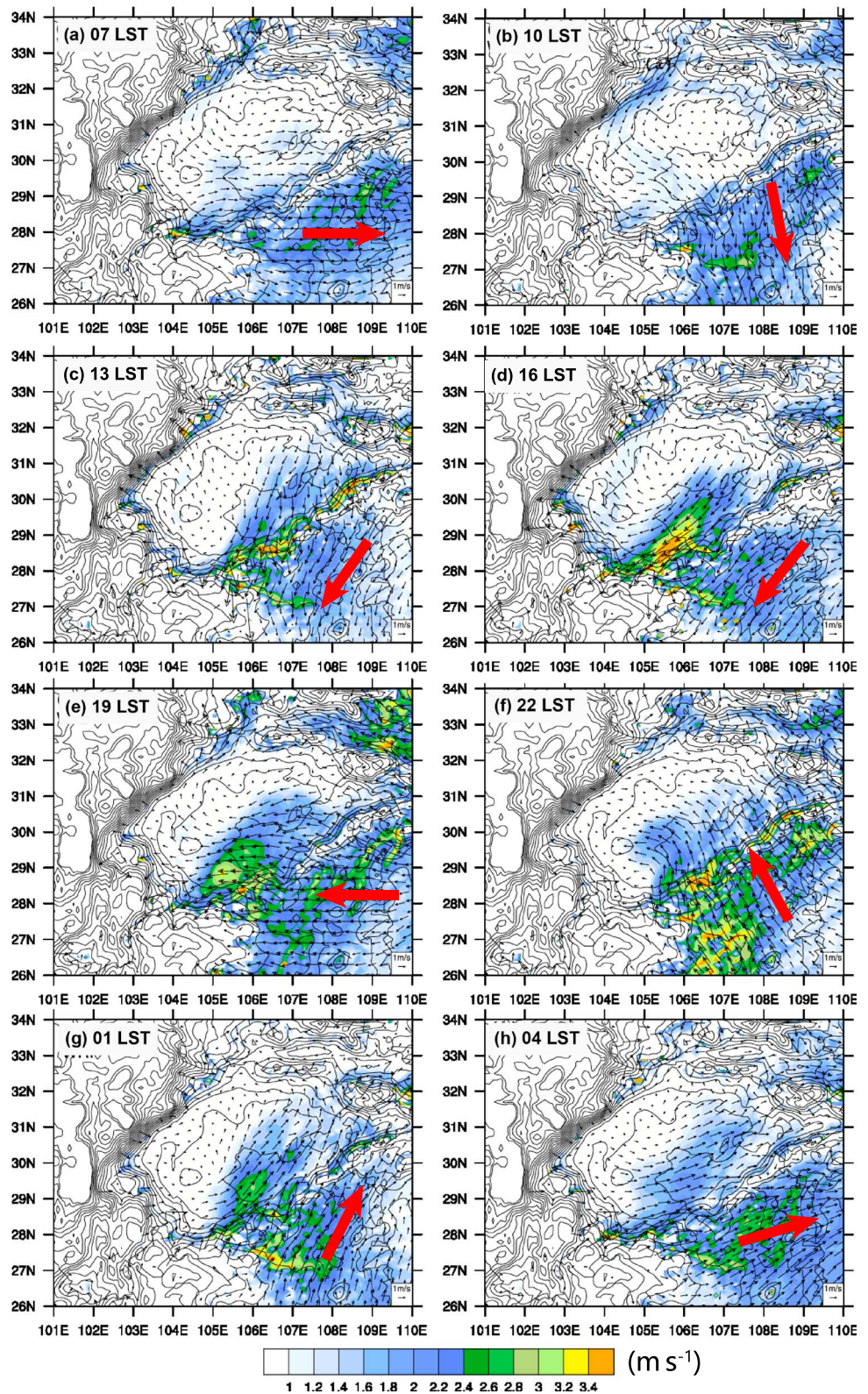


Figure 7. The WRF_NJU-simulated 850-hPa perturbation wind vectors and the horizontal perturbation wind speed (shaded), from (a) 07 LST to (h) 04 LST, every 3 hr in 2013 summer. Perturbations at each grid point are computed by subtracting the daily mean values at that grid point. The thick open arrow in each panel indicates the general direction of the perturbation wind vectors over the Yunnan-Guizhou Plateau.

geostrophic wind. In this study, due to the presence of complex topography, geostrophic winds are difficult to estimate. The deviation from the daily mean is therefore used as a proxy of the ageostrophic wind. Other studies, such as G. Chen et al. (2013) and Zhang et al. (2014) have taken a similar approach. Here we also point out that apart from the Blackadar (1957) inertial oscillation mechanism, the sloping-terrain/thermal wind adjustment mechanism of Holton (1967) considered in the generalized models of Shapiro et al. (2016) and Du and Rotunno (2014) may also have some, though we believe less important, role to play.

In terms of the deviation wind vectors, at 07 LST through 13 LST, the wind vectors are directed out of SB across its southeast rim (Figures 7a–7c), which effectively pull low-level air out of the basin, creating low-level flow divergence. On the contrary, at 19 LST through 01 LST, the winds are directed into the basin, with the winds being strongest and directed at almost 90° angles cross the rim into the basin at 22 LST (Figure 7f), providing most moisture transport into the basin as well as producing boundary layer flow convergence within the basin. Compared to the magnitude and direction changes of flows across the southeast rim, flow changes near the other rims of the basin are much smaller.

Adding the deviation winds in Figure 7 to the daily mean winds in Figure 6 gives us the total winds shown in Figure 8. We can see at 22 LST (Figure 7f) and 02 LST (Figure 7g) when the deviation winds are strong and southerly, and in similar directions as the mean winds (Figure 6), the total winds are the strongest (Figures 8f and 8g) at 850 hPa; the strong total winds transport a large amount of moisture into the basin, leading to, not surprisingly, the heaviest precipitation at 02 LST as seen in Figure 3. In terms of total winds, the wind vectors oscillate between south southwesterly to south southeasterly, while the changes in wind speed are larger. At 10 and 13 LST, the outward directed deviation flows make the total winds into the basin the weakest during the day, corresponding to precipitation minimum.

Again, the deviation winds have an obvious 24-hr cycle, and the periodic clockwise rotation of the deviation winds is consistent with the inertial oscillation theory of Blackadar, and the boundary layer initial oscillations are most evident in diurnal changes of boundary layer LLJ. To see if this is indeed true, we plot in Figure 9a vertical profiles of the mean horizontal wind speed, averaged over grid points within the red rectangle of Figure 6, and also in Figure 9b the wind component normal to plane A of the white budget analysis box shown in Figure 1, for different times of the day. We can see that in both versions, a prominent LLJ having maximum wind speed at ~850 hPa is evident. It has similar intensity between 21 and 01 LST in terms of total wind (Figure 9a) and has larger variations during the period in terms of normal wind speed (Figure 9b). The total wind speed reaches its maximum at 23 LST while the normal wind peaks at 22 LST. In the early afternoon at 1300 LST, the jet is much weaker, which according to Blackadar theory is due to intense vertical mixing within the boundary layer; the boundary layer flow is slowed down by surface friction in the presence of strong vertical mixing in the afternoon unstable convective boundary layer.

To give a more direct view of the diurnal cycle of the deviation winds, a hodograph of average deviation wind vectors within the red rectangle in Figure 6 at 850 hPa are shown in Figure 10 at hourly intervals. In this plot, tips of the deviation wind vectors are connected to form a hodograph. With the dots forming a closed circle, the deviation winds show continuous clockwise rotation, a behavior that again agrees with the prediction of the Blackadar boundary layer inertial oscillation theory for boundary layer LLJ. Similar conclusions were made about diurnal oscillations of southerly monsoon flows into the Meiyu frontal zone in Xue et al. (2018). From the hodograph, we can again see that at 22 LST, the deviation wind directed into SB through its southeast rim is the strongest. Now that we have shown that there are strong diurnal changes of flow into SB from the southeast side of SB, and such diurnal changes can be explained well by the Blackadar inertial oscillation theory, we want to see more quantitatively the role of such flow changes in controlling the precipitation diurnal cycles in SB.

4.3. Relation of Low-Level Moisture Fluxes and Net Flux Convergence With SB Rainfall

To investigate the contributions and roles of circulations in and around SB, we examine moisture fluxes into a control volume enclosed by the white box shown in Figure 1. The box boundaries are chosen to be located at the edge of the basin, at the foot of TP and YGP, Dabashan Mountains to the north, and eastern YGP to the southwest. Any thermally given upslope and downslope circulations would affect convergence and

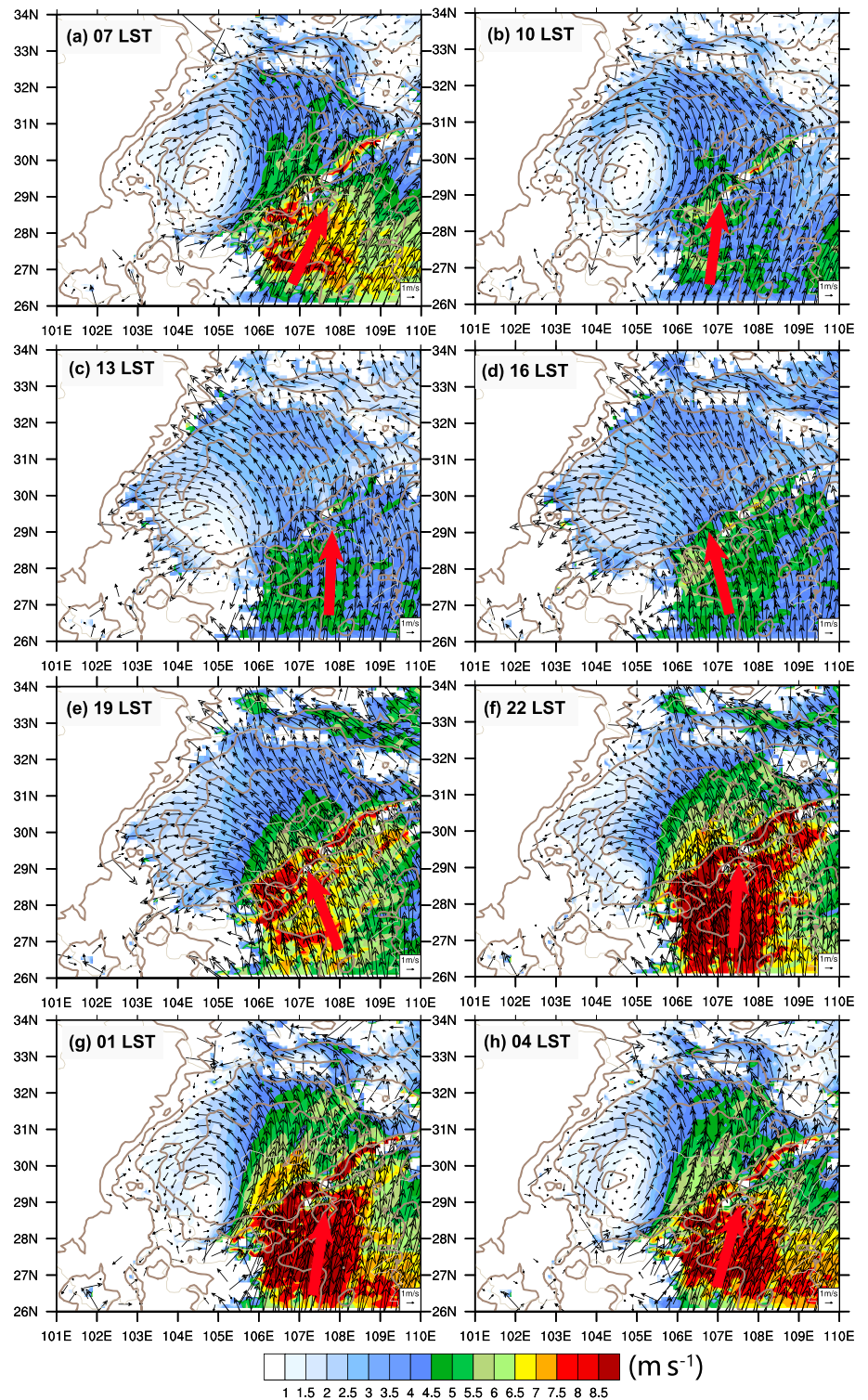


Figure 8. The average WRF_NJU-simulated 850 hPa wind vectors and the horizontal wind speed (shaded), from (a) 07 LST to (h) 04 LST, every 3 hr, in 2013 summer. The terrain is superimposed as contours. The thick red arrow in each panel indicates the general direction of the perturbation wind vectors over the Yunnan-Guizhou Plateau.

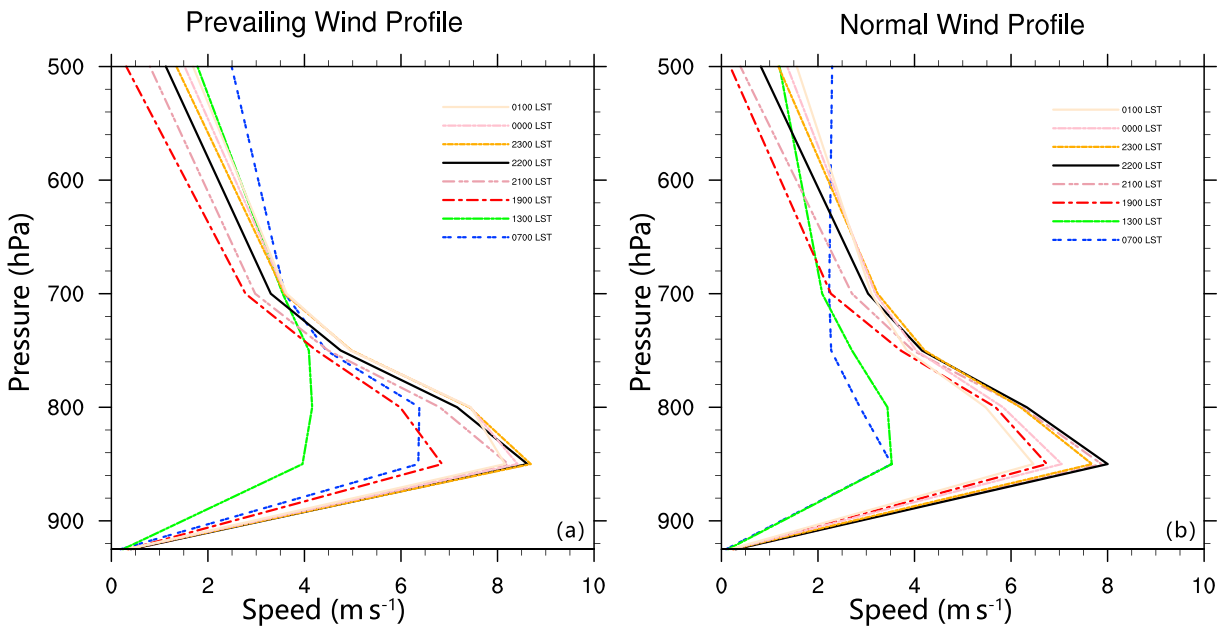


Figure 9. Profiles of the horizontal wind speed averaged within the box on the Yunnan-Guizhou Plateau (see in Figure 6).

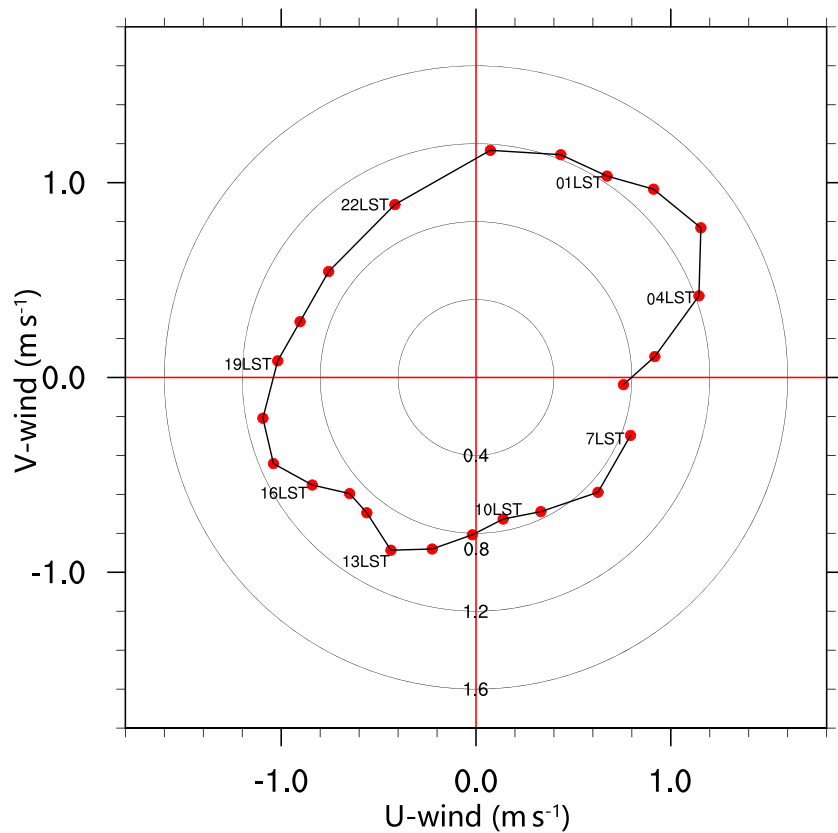


Figure 10. Hodograph of mean deviation winds in the Sichuan Basin (red box in Figure 6). The dots on the curves correspond to the tips of the deviation vectors.

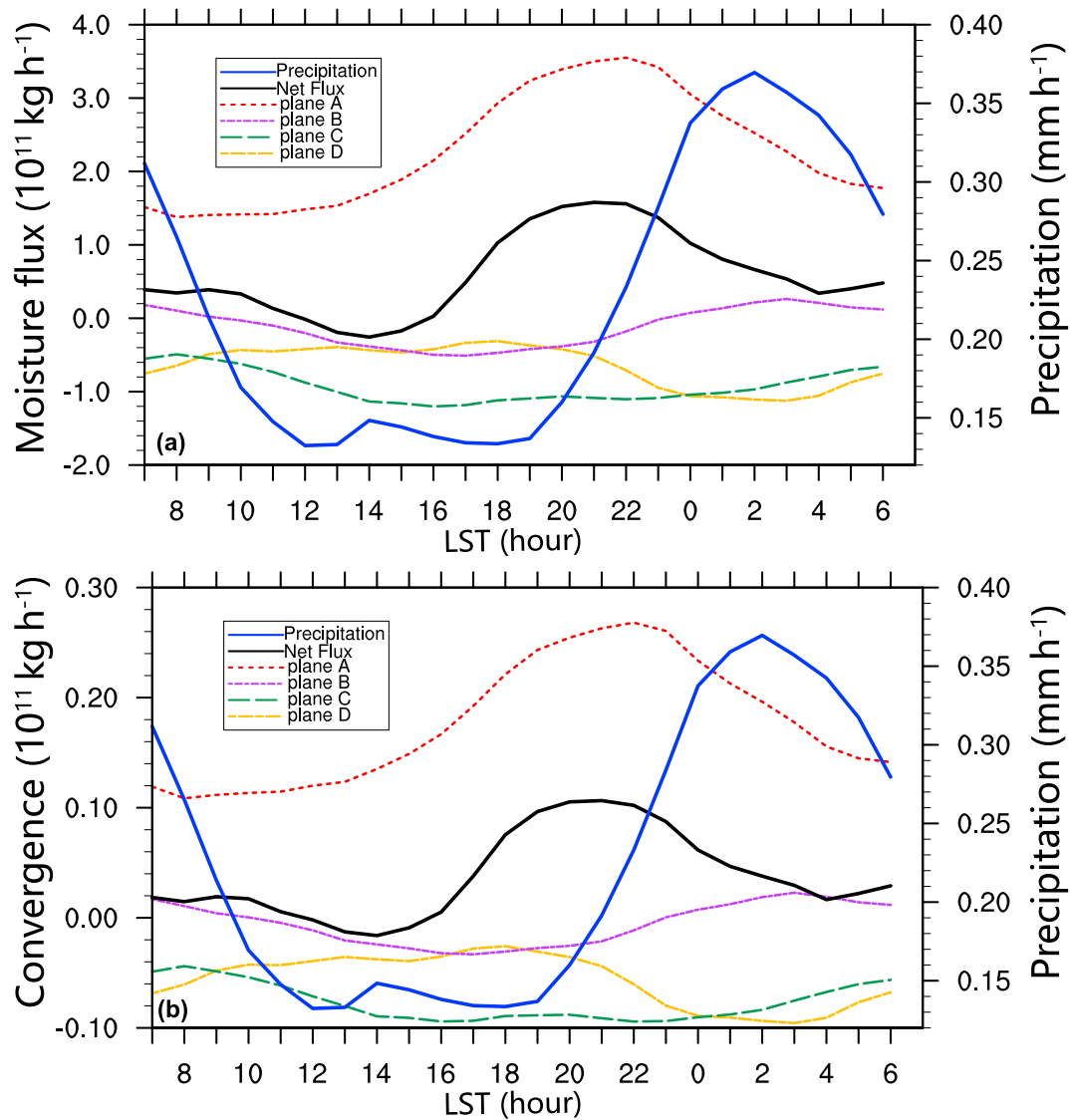


Figure 11. Spatial- and temporal-averaged time series of WRF_NJU-simulated (a) moisture flux and (b) wind convergence for net fluxes, four planes separately, and precipitation in the basin in 2013 summer. The solid black line represents the net flux of the box in Figure 1. The red dashed line represents moisture flux for plane A; the purple dashed line represents for plane B; the green dashed line represents plane C, the yellow dashed line represents plane D, and the blue line represents the precipitation in the Sichuan Basin.

divergence inside the basin, and moisture fluxes into the basin, providing low-level dynamic forcing and moisture source for basin precipitation. The variations of low-level flows including LLJ through the southeast boundary would also have significant effects.

We plot in Figure 11a the moisture fluxes through the four boundaries of the control volume (the white box in Figure 1) and the net moisture flux into the basin, together with the hourly forecast precipitation. The moisture fluxes are calculated according to

$$Q = \int_{z_s}^{z_t} \int_{x_1}^{x_2} (\rho q_v V_n) dx dz,$$

where ρ , q_v , and V_n are air density, water vapor mixing ratio, and velocity normal and into the boundary, respectively. The integration is over the length of the boundary from x_1 to x_2 , and from the ground surface z_s to $z_t = 2$ km AGL. The flux directed into the basin is positive.

Figure 11b is the same as Figure 11a except that air mass fluxes are plotted instead of moisture fluxes. The air mass fluxes are calculated according to

$$F = \int_{z_0}^{z_1} \int_{x_1}^{x_2} (\rho V_n) dx dz.$$

The net low-level air mass convergence into the basin is equivalent to net air mass flux exiting the top boundary of the budget control volume, representing low-level upward dynamic forcing/lifting.

The moisture fluxes through plane A on the southeast side (red curve in Figure 11a) has a distinct nocturnal peak at 22 LST and much lower values between 04 and 15 LST with a minimum at 09 LST; these are consistent with the diurnal variations of normal wind speed profiles shown in Figure 9b. The moisture fluxes through plane A are much larger than those through other three boundaries and remain positive (into the basin) for the entire day, because of the strong persistent prevailing winds from the south there.

The net flux in SB (black line in Figure 11a) has a very similar variation as the flux through plane A. They both have a distinct peak at 22 LST, indicating that the nocturnal LLJ through plane A plays the most important role in determining the net flux peak. The minimum of the net fluxes occurs at 14 LST, caused by the similar decrease trends of the fluxes through planes B and C from early morning through late afternoon, and the relatively small variations in fluxes through plane D up to the evening and through plane A up to early afternoon. The total fluxes through plane C are always negative, or out of the box, corresponding to the overall southeasterly flow directions there (see Figure 9). The downward trend of fluxes through plane C from morning through the afternoon should be associated with the daytime upslope flow due to thermal effect which draws more air out of the basin (Figure 11a green line). The total flux through plane B or at the foot of YGP oscillates between positive and negative values (Figure 11a purple line), which is the reflection of upslope and downslope flows between day and night in the absence of strong background winds (see Figures 4b and 4d).

The diurnal variation of the net moisture flux into SB (black line in Figure 11a) has a close relation with the diurnal variation of hourly precipitation (blue line in Figure 11a). Both have single peak and single minimum within a day. The net flux peak at 22 LST is ~4 hr earlier than the precipitation peak at 02 LST, suggesting that the much enhanced boundary layer moisture flux convergence into the basin is forcing precipitation within the basin, causing the precipitation to peak a few hours after the convergence peak is reached. Note that as long as there is positive net convergence into the basin, new precipitation could be forced, so the development of precipitation should not stop after the convergence peak is reached and it takes some time for the precipitation to fall to the ground after the development of upward motion. Xue et al. (2018) found similar time delay in precipitation peak compared to low-level moisture convergence peak within Meiyu frontal systems and concluded the important forcing mechanism by nocturnal LLJ associated with inertial oscillations.

In terms of the relative role of flux variations along the four boundaries in modulating precipitation in the basin, the magnitude of diurnal variations at each boundary is the key. The total flux through plane A changes by nearly 4×10^{11} kg/hr between maximum and minimum, while changes in fluxes through other planes are generally around 2×10^{11} kg/hr. Furthermore, the sum of fluxes through planes B–D changes only by about 2×10^{11} kg/hr throughout the day, being essentially constant except for between 10 and 17 LST when it has lower values. This can be seen in terms of the difference between the flux through plane A (red line) and the net flux (black line)—they are more or less parallel except for between 10 and 17 LST. So the sum of the three fluxes have negative net effect between late morning and late afternoon, drawing moist air out of the basin, which must have been because of the thermally driven upslope flows. Such upslope flows and the negative perturbation winds out of the basin through plane A during the day (Figure 7) should be responsible for precipitation minimum during the day.

From the late afternoon into the evening, the flux through plane A increases dramatically after 15 LST (Figure 11a) because of the development of perturbation winds directed toward plane A into the basin (Figure 7). The fluxes through planes B and C also increase after 17 LST, near the time of sunset and reach maximum between 3 and 6 LST. The fact that these fluxes reach maximum after the precipitation peak is reached at 02 LST, and the magnitude of the changes are relatively small suggests that thermally driven downslope flows from the slopes of TP and YGP and other surrounding mountains into the basin is of at most secondary role in producing the nighttime precipitation peak around 02 LST.

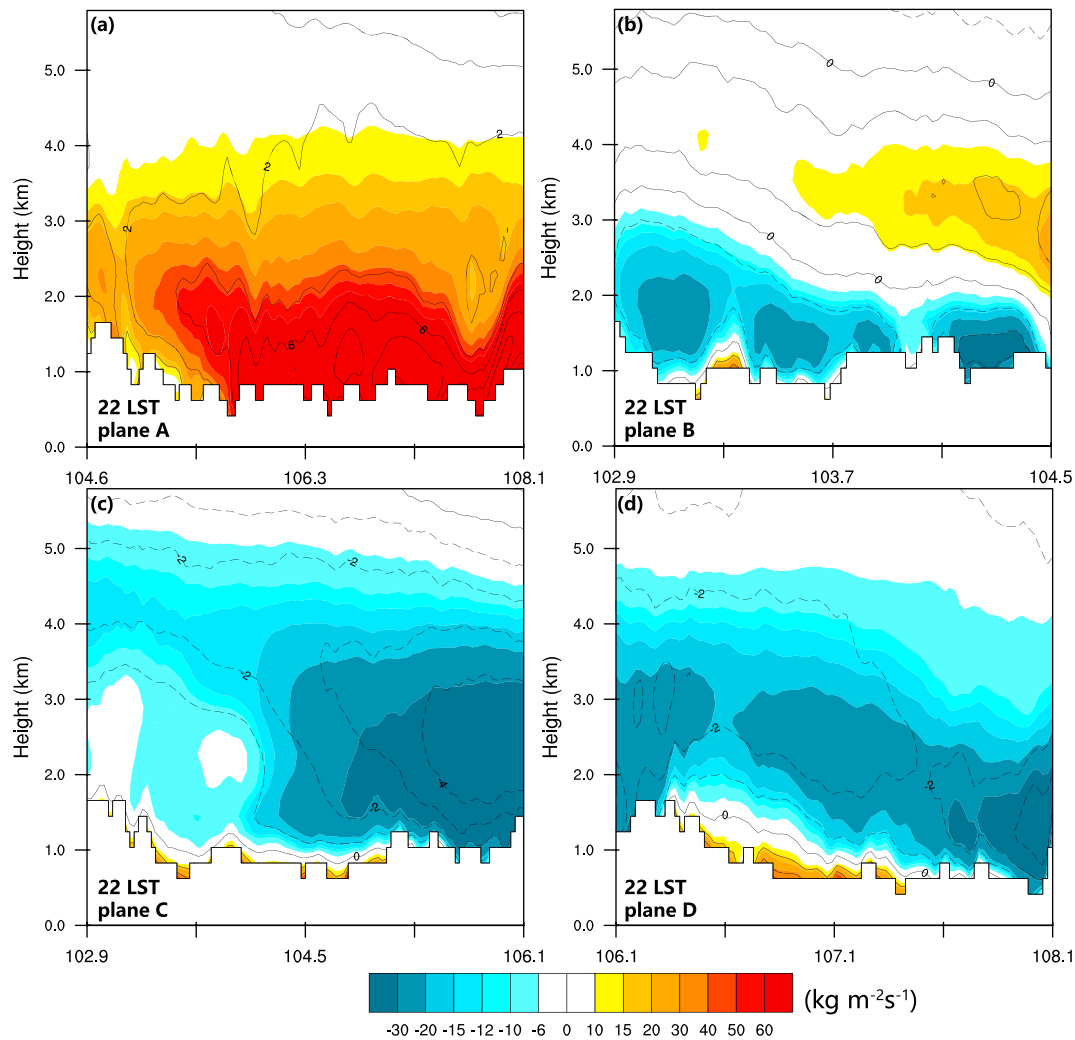


Figure 12. The mean moisture fluxes (shading) through the four planes or boundaries (plane A, B, C and D) of the budget control volume (in Figure 1) at 22 LST, together with the speed of horizontal wind perpendicular to the plane (contours).

The air mass fluxes in Figure 11b tell a very similar story as moisture fluxes in Figure 11b; the air mass fluxes have very similar diurnal variations as the moisture fluxes, with that through the southeast boundary having a very similar trend as that of net mass flux, although the mass flux reaches its peak earlier at around 20 LST, and remains positive throughout the night. The net mass flux also peaks at 22 LST (Figure 11b), suggesting that it is indeed the low-level dynamic forcing modulated primarily by the flows through the southeast boundary that controls the diurnal variation of precipitation within the basin.

To see more clearly how wind and moisture fluxes are distributed in the lower atmosphere through the control volume boundaries or the four planes, we show in Figures 12 and 13 these fields at 22 and 13 LST, about the times of peak and minimum net moisture fluxes, respectively (Figure 11). At 22 LST, the majority of the net moisture flux goes into the basin through the southeast boundary (Plane A, Figure 12a) and some of it leaves the basin from the northeast and northwest boundaries (Plane C and D) given the prevailing wind direction. The horizontal wind maximum in Plane A is found at about 500 m AGL and is the strongest in the middle section of Plane A, agreeing with results shown in Figures 9 and 10. Strong moisture fluxes are found extending to ~4 km AGL. In Planes B, C, and D, a very shallow layer of positive moisture fluxes is found near the surface, which is due to the night downslope drainage flows (Figure 12). Clearly, these fluxes contribute to only a small fraction of the total fluxes through these planes, therefore do not constitute the primary forcing mechanism of nighttime precipitation peak.

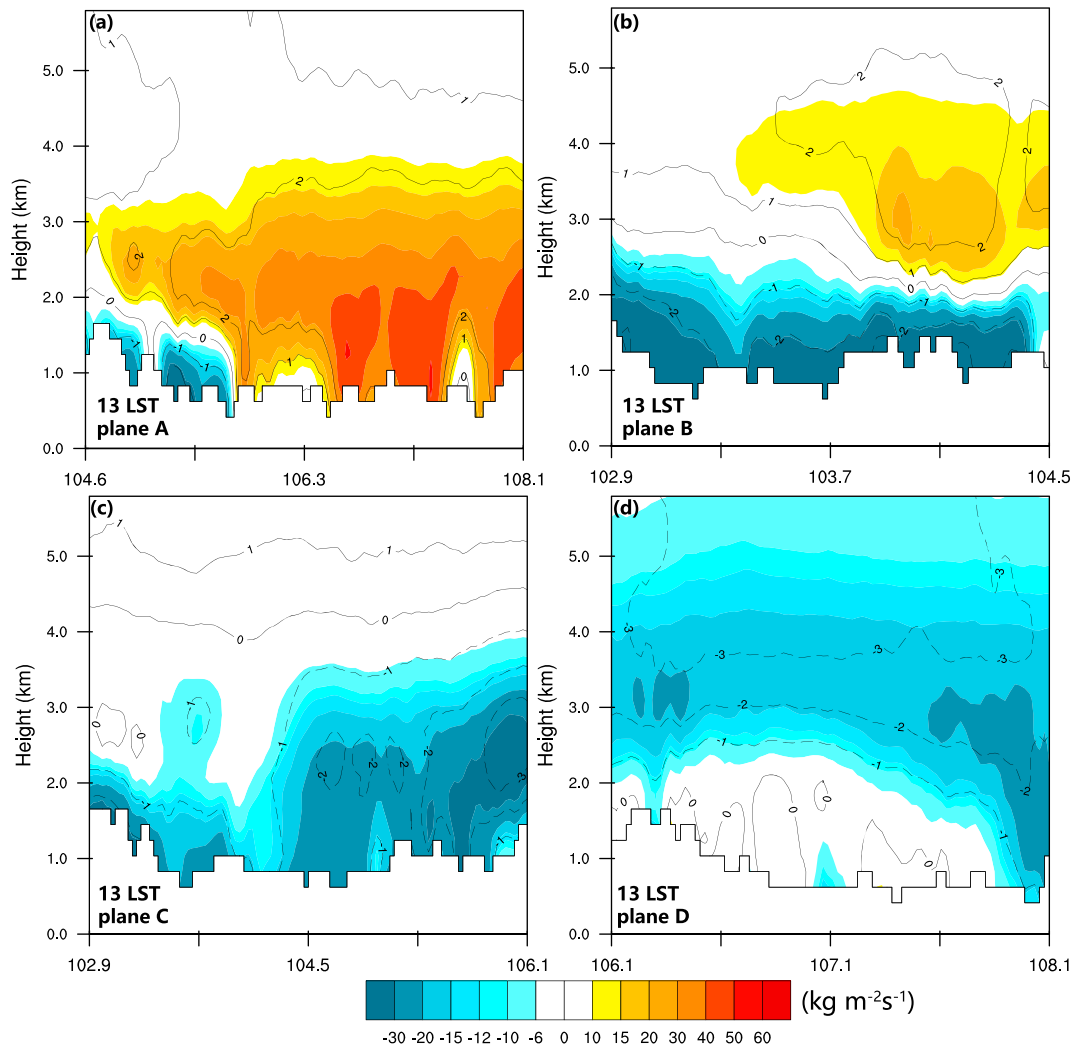


Figure 13. As in Figure 12 but for 13 LST.

In Plane B, outward moisture flux dominates from surface to nearly 2 km AGL at 22 LST (Figure 13b), consistent with the horizontal wind field at the foot of the YGP (Figure 8f); a cyclonic circulation center is found near the southeast corner of SB resulting in northeasterly upslope flows in that region (Figure 8f). Above 2 km AGL in the right half of Plane B, the moisture flux turns positive (Figure 12b); this should be associated with the prevailing southerly winds that had not been significantly modified by the terrain.

At 13 LST, the wind normal to Plane A is more or less uniform below 3 km AGL in the right portion of the plane (Figure 13a) and is much weaker than that at 22 LST (Figure 12a). This is due to the development of a daytime well-mixed boundary layer that erodes the boundary layer LLJ (c.f., Figure 9). The negative flux near the lower left corner of Plane A should be due to upslope flows that develop there. The patterns of fluxes in Plane B are similar between 13 and 22 LST, although the shallow downslope flows near the surface is replaced by strong upslope flows, giving negative net flux at this time (c.f. Figure 11). The flux through Plane C is negative or outward at 13 LST everywhere, but the flux corresponding to the southeasterly prevailing winds is shallower and weaker (Figure 13c) than that at 22 LST (Figure 12c), indicating that the boundary layer upslope flow on the eastern slope of TP is not strengthened but weakened during the day, apparently due to the overall weakening of the LLJ coming from southeast of SB. Right on the TP slope the flow is upslope instead of downslope. In Plane D, the downslope flow near the surface at 22 LST has disappeared, leaving very weak fluxes below 2 km, while the flux above 2 km is outward, due to again the

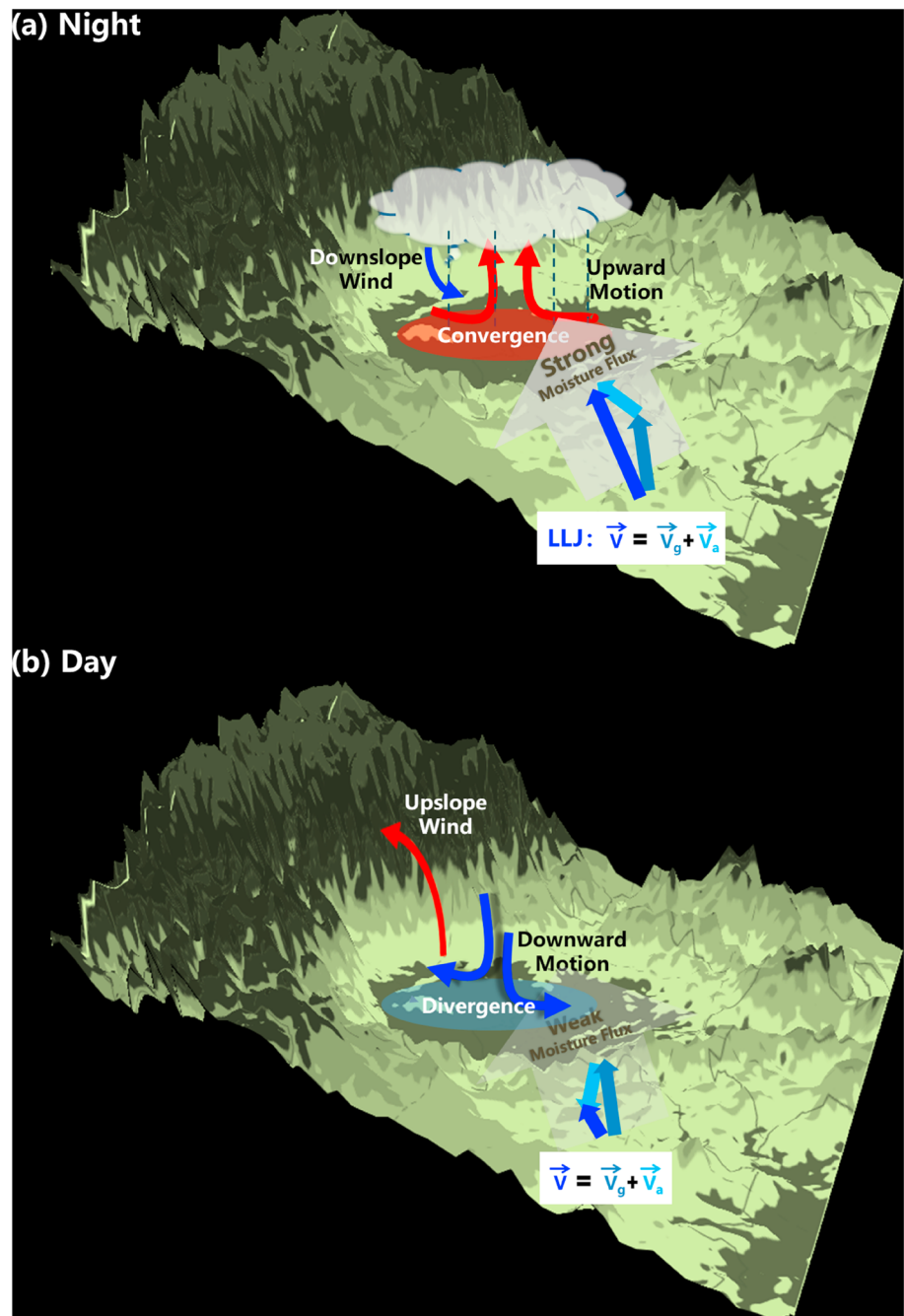


Figure 14. A conceptual model of diurnal precipitation variations including peak nighttime precipitation over Sichuan Basin. The wind over eastern Yunnan-Guizhou Plateau, including the daily mean quasi-geostrophic wind \vec{V}_g (navy blue vector), the total wind \vec{V} (the sky-blue vector), and the perturbation ageostrophic wind \vec{V}_a (light blue vector) at the time of precipitation peak shortly after midnight (a), and during daytime precipitation minimum (b). The wide light gray arrow indicates the moisture flux into Sichuan Basin. Updrafts and downdrafts as well as upslope and downslope flows are represented by the red and blue curved arrows. Strong net low-level convergence within Sichuan Basin forces precipitation at night while low-level divergence dissipates and suppress daytime precipitation. LLJ = low-level jet.

prevailing wind direction there (Figure 13d). Overall, the change in the moisture flux through Plane A is most significant between day and night, and the change is mostly due to the change in the boundary layer LLJ intensity. The nighttime downslope flows due to mountain slope cooling is very shallow, and should only contribute to a small portion of the total flux changes through the control volume boundaries.

All of the evidences presented so far support our conclusions that the diurnal variations in the boundary layer LLJ over eastern YGP to the southeast of SB due to boundary layer inertial oscillations play the most important role in controlling the diurnal cycles and especially the maximum of precipitation shortly after midnight in SB. The thermal upslope and downslope circulations due to daytime heating and nighttime cooling of the surrounding mountains and plateaus play only secondary roles. The facts that the opening of SB faces southeast and the clockwise rotating boundary layer perturbation wind vector becomes normal to the southeastern boundary of SB and reaches maximum speed at 22 LST explain well why the precipitation peak is reached shortly after midnight local time. In fact, the mean perturbation wind vector becomes directed out of the southeastern boundary of SB after 02 LST (Figure 10) while the fluxes into SB through some of the other boundaries (Figure 11) continue to increase after 02 LST but the precipitation within the basin stops increasing after 02 LST (Figure 11) convincingly supports our conclusions about the primary role of LLJ diurnal oscillations over those of topographically forced thermal circulations.

5. Summary and Conclusions

The SB is one of the heavy precipitation centers in China in the warm season. It is well known that precipitation in SB is dominated by that at night while daytime precipitation in SB is suppressed. The conventional wisdom is that the nighttime precipitation is forced by downslope flows off the TP to the west, and the YGP to its south converging into the basin at night, while during the day, solenoidal circulations of opposite directions produce downward motion and low-level divergence within the basin, suppressing precipitation. Nighttime cloud top radiative cooling had been suggested to be another possible cause. Studies have also noticed enhancement of southerly flows in the form of LLJ into SB and suggested its possible rule in SB nighttime precipitation.

In this paper, precipitation forecasts over June through August of 2013 produced by the WRF model at a 4 km grid spacing covering the entire China are used to study precipitation diurnal cycles within SB, China. The average (over the 3 months) hourly precipitation forecasts are first compared to dense rain gauge observations and good agreements are found in the spatial distribution as well as diurnal changes in the precipitation with observations. A single peak in daily precipitation is found at around 02 LST, while precipitation during most of the day is much weaker. The key mechanism of SB precipitation diurnal cycle and in particular of nighttime peak is studied by examining the vertical and horizontal circulations and their changes through the day and night, the low-level moisture fluxes through four sides of SB and the net moisture fluxes into SB, and their relationships with the precipitation diurnal changes. The diurnal changes of the LLJ from the southeast over the eastern YGP that feeds SB, and the perturbations winds from daily mean at the jet level, are examined and the causes of such diurnal changes are discussed. Based on these analyses, we conclude that the diurnal changes of the southerly LLJ play the most important role in controlling the precipitation diurnal cycles within SB.

Specific findings are listed as follows:

1. The diurnal precipitation over SB has a prominent peak around 02 LST in the summer months of 2013, and it is reproduced well by the WRF 4 km forecasts used in this study.
2. The low-level total moisture flux across the southeast boundary of SB has the largest diurnal variations, and its variations are almost exactly in phase with those of the net moisture flux convergence into SB; both peak at around 22 LST, 4 hr before the precipitation peak, and both have minimum before early afternoon. The magnitudes of diurnal variations of low-level moisture fluxes through the other three boundaries of SB are only about one third that of flux through the southeast boundary.
3. The nighttime downslope flows and daytime upslope flows on the eastern slope of TP and northern slope of YGP are very shallow, and contribute only a small fraction of the total fluxes through the SB boundaries placed at the foot of TP and YGP, and hence a small fraction to the net moisture flux convergence or divergence in SB, and to the modulation of precipitation diurnal changes in SB.
4. The vertical wind profiles over eastern YGP south of SB exhibit prominent nocturnal LLJ peaking at about 500 m AGL (850 hPa) and at 22–23 LST, and the LLJ is much weaker in the afternoon at 13 LST.
5. The perturbation wind vector from the daily mean at the peak LLJ level exhibits prominent clockwise rotation, and is large and points in the northwest direction that is perpendicular to the southeast boundary of SB. Such strong perturbation winds act to force the most amount of moist air into SB at 22 LST

- (starting from 15 LST through 02 LST) while pulling the most amount of air out of SB in early morning through earlier afternoon (from 02 LST through 15 LST). The cumulative effect of such perturbation flows is enhanced nighttime precipitation peaking at 02 LST and suppressed precipitation during the day.
6. The prominent diurnal oscillations in the strength of LLJ, including the nighttime intensity, can be explained well by the boundary layer inertial oscillation theory of Blackadar (1957). Additional terrain effects, as advocated by Holton's (1967) LLJ theory, may have some contributions to the LLJ diurnal oscillations, but their contributions are believed to be secondary.

Based on our results, a conceptual model is proposed and illustrated in Figure 14. At night (Figure 14a), the plateaus and mountains around SB, including TP and YGP, are colder than the air over SB so that downslope drainage flows develop on the plateau and mountain slopes. The flows converge into SB and help to enhance low-level convergence within SB that promotes nighttime precipitation. However, because such flows are very shallow, they contribute only a small amount to the net convergence within SB. To the southeast of SB over the lower YGP of about 1 km height, strong super-geostrophic LLJ (bright blue straight arrow in Figure 14a) develops late into the evening, as the boundary layer flow is freed from the effects of surface friction and accelerates past the geostrophic balance. The low-level moisture transport into SB and the moisture convergence within SB are maximized at around 22 LST as the ageostrophic perturbation wind vector (navy blue arrow) rotates into the southeast-boundary-normal direction. The strong net convergence within SB promotes nighttime precipitation that peaks at around 02 LST. The precipitation weakens after 02 LST as the perturbation winds rotate away from the SB boundary, even though the downslope drainage flows continue throughout the night.

During the day (Figure 14b), the slopes of the surrounding mountains are heated up and upslope flows develop, drawing air out of SB, contributing to the development of low-level divergence within SB. The upslope flows are again relatively shallow, however. During the day, the LLJ over eastern YGP is sub-geostrophic, due to slowing down by surface friction in the presence of unstable boundary layer eddy mixing. The perturbation winds from the daily mean (navy blue vector in Figure 14b) point in the southward direction, away from SB, and hence acts to draw air out of SB. Working together with the upslope flows, a net low-level moisture divergence is created within SB, causing nighttime precipitation to dissipate, and new precipitation to fail to develop in the afternoon.

This study is primarily based on average of hourly forecasts over three summer months of 2013, and the results represent the dominant behaviors of precipitation within SB in that year. While we believe the main conclusions obtained in this paper are representative and robust, since they agree with available observational data and behaviors documented in other climatological studies. Further studies will try to separate days strongly influenced by southerly LLJ, and days influences coming from the north or west of SB are stronger. The latter include days when weather and/or convective systems moving into SB from the Plateau; migration into the basin of convective systems that developed over the Plateau in the afternoon may be a significant contributor to nighttime precipitation in the basin on some days. Additional dynamical effects of terrain on the distribution of precipitation in and around SB should also be investigated.

Finally we point out that certain studies, including Bao et al. (2011), Sun and Zhang (2012), and Zhang et al. (2014) have emphasized the importance of mountain-plain solenoidal (MPS) circulations on precipitation and their diurnal changes east of the TP. These studies did not quantitatively access the contribution of diurnal changes in LLJ to the diurnal cycles of precipitation relatively to that of MPS circulations. Their vertical MPS circulations over the TP slopes were not shallow in their plots, presumably due to the relatively low vertical resolution of their data, the averaging they performed on the wind fields over a latitudinal band (despite the presence of irregular terrain), and for some of the fields the spatial filtering that was applied. In contrast, the study of Xue et al. (2018) showed that the boundary layer inertial oscillations play a controlling role in precipitation diurnal cycles during the Meiyu season over the plains east of the TP. Further studies on this topic are clearly needed.

References

- Bao, X., Zhang, F., & Sun, J. (2011). Diurnal variations of warm-season precipitation east of the Tibetan Plateau over China. *Monthly Weather Review*, 139(9), 2790–2810. <https://doi.org/10.1175/mwr-d-11-00006.1>
- Blackadar, A. K. (1957). Boundary layer wind maxima and their significance for the growth of nocturnal inversions. *Bulletin of the American Meteorological Society*, 38, 283–290. <https://doi.org/10.1175/1520-0477-38.5.283>

Acknowledgments

This work was primarily supported by the National Key Research and Development Program of China (2018YFC1507302), the Natural Science Foundation of China grant 41730965 and the Foundation of China Meteorological Administration special (grant GYHY201506006). This work is also supported by the National 973 Fundamental Research Program of China (2013CB430103). The gridded data at reduced resolution including rain gauge observations and WRF forecasts are available online (https://pan.baidu.com/s/19VW90a7pwhwg_gBVgl4r3A). For more detailed data, please contact us via email.

- Bonner, W. D. (1966). Case study of thunderstorm activity in relation to the low-level jet. *Monthly Weather Review*, *94*, 167–178. [https://doi.org/10.1175/1520-0493\(1966\)094<0167:CSOTAI>2.3.CO;2](https://doi.org/10.1175/1520-0493(1966)094<0167:CSOTAI>2.3.CO;2)
- Chen, G., Sha, W., Sawada, M., & Iwasaki, T. (2013). Influence of summer monsoon diurnal cycle on moisture transport and precipitation over eastern China. *Journal of Geophysical Research: Atmospheres*, *118*, 3163–3177. <https://doi.org/10.1002/jgrd.50337>
- Chen, G.-X., Sha, W., & Iwasaki, T. (2009). Diurnal variation of precipitation over southeastern China: Spatial distribution and its seasonality. *Journal of Geophysical Research*, *114*, D13103. <https://doi.org/10.1029/2008JD011103>
- Chen, H., Yu, R., Li, J., Yuan, W., & Zhou, T. (2010). Why nocturnal long-duration rainfall presents an eastward-delayed diurnal phase of rainfall down the Yangtze River valley. *Journal of Climate*, *23*(4), 905–917. <https://doi.org/10.1175/2009jcli3187.1>
- Collins, W. D. (2004). Description of the NCAR community atmosphere model (CAM 3.0).
- Du, Y., & Rotunno, R. (2014). A simple analytical model of the nocturnal low-level jet over the Great Plains of the United States. *Journal of the Atmospheric Sciences*, *71*(10), 3674–3683. <https://doi.org/10.1175/jas-d-14-0060.1>
- Du, Y., Zhang, Q., Chen, Y. L., Zhao, Y., & Wang, X. (2014). Numerical Simulations of Spatial Distributions and Diurnal Variations of Low-Level Jets in China during Early Summer. *Journal of Climate*, *27*(15), 5747–5767.
- Du, Y., Zhang, Q., Ying, Y., & Yang, Y. (2012). Characteristics of low-level jets in Shanghai during the 2008 and 2009 warm seasons as inferred from wind profiler radar data. *Journal of the Meteorological Society of Japan*, *90*, 891–903. <https://doi.org/10.2151/jmsj.2012-603>
- He, M.-Y., Liu, H.-B., Wang, B., & Zhang, D.-L. (2016). A modeling study of a low-level jet along the Yun-Gui Plateau in south China. *Journal of Applied Meteorology and Climatology*, *55*(1), 41–60. <https://doi.org/10.1175/jamc-d-15-0067.1>
- Higgins, R. W., Yao, Y., Yarosh, E. S., Janowiak, J. E., & Mo, K. C. (1997). Influence of the Great Plains low-level jet on summertime precipitation and moisture transport over the Central United States. *Journal of Climate*, *10*, 481–507. [https://doi.org/10.1175/1520-0442\(1997\)010<0481:IOTGPL>2.0.CO;2](https://doi.org/10.1175/1520-0442(1997)010<0481:IOTGPL>2.0.CO;2)
- Holton, J. R. (1967). The diurnal boundary layer wind oscillation above sloping terrain. *Tellus*, *19*, 199–205. <https://doi.org/10.1111/j.2153-3490.1967.tb01473.x>
- Hu, L., Deng, D., Gao, S., & Xu, X. (2016). The seasonal variation of Tibetan Convective Systems: Satellite observation. *Journal of Geophysical Research: Atmospheres*, *121*, 5512–5525. <https://doi.org/10.1002/2015JD024390>
- Huang, D.-Q., Zhu, J., Zhang, Y.-C., Wang, J., & Kuang, X.-Y. (2015). The impact of the East Asian subtropical jet and polar front jet on the frequency of spring persistent rainfall over southern China in 1997–2011. *Journal of Climate*, *28*(15), 6054–6066. <https://doi.org/10.1175/jcli-d-14-00641.1>
- Huang, H. L., Wang, C. C., Chen, T. J., & Carbone, R. E. (2010). The role of diurnal solenoidal circulation on propagating rainfall episodes near the eastern Tibetan Plateau. *Monthly Weather Review*, *138*(7), 2975–2989. <https://doi.org/10.1175/2010MWR3225.1>
- Jin, X., Wu, T., & Li, L. (2012). The quasi-stationary feature of nocturnal precipitation in the Sichuan Basin and the role of the Tibetan Plateau. *Climate Dynamics*, *41*(3–4), 977–994. <https://doi.org/10.1007/s00382-012-1521-y>
- Li, J., Yu, R., & Zhou, T. (2008). Seasonal variation of the diurnal cycle of rainfall in southern contiguous China. *Journal of Climate*, *21*(22), 6036–6043. <https://doi.org/10.1175/2008jcli2188.1>
- Lin, J., & Yang, G. (2014). Recent 30 years spatial and temporal characteristic analysis, in China, Meteorol Month 07), 816–826.
- Lin, X., Randall, D. A., & Fowler, L. D. (2000). Diurnal variability of the hydrologic cycle and radiative fluxes: Comparisons between observations and a GCM. *Journal of Climate*, *13*(23), 4159–4179. [https://doi.org/10.1175/1520-0442\(2000\)013<4159:DVOTHC>2.0.CO;2](https://doi.org/10.1175/1520-0442(2000)013<4159:DVOTHC>2.0.CO;2)
- Luo, Y., Qian, W., Zhang, R., & Zhang, D. L. (2013). Gridded hourly precipitation analysis from high-density rain gauge network over the Yangtze-Huai Rivers basin during the 2007 Mei-Yu season and comparison with CMORPH. *Journal of Hydrometeorology*, *14*(4), 1243–1258. <https://doi.org/10.1175/JHM-D-12-01133.1>
- Lv, J. (1942). Nocturnal precipitation in Bashan. *Acta Meteorologica Sinica*, *61*, 36–53.
- Mai, Z., Fu, S., Sun, J., & Hu, L. (2019). A sixteen-year statistical study of mesoscale convective systems generated over the Tibetan Plateau: Key features and their relationship to precipitation and southwest vortices. *Journal of Climate*.
- Markowski, P. M., & Richardson, Y. (2010). *Mesoscale meteorology in midlatitudes* (p. 430). Chichester, UK: Wiley-Blackwell. <https://doi.org/10.1002/9780470682104>
- Morrison, H., Curry, J. A., Shupe, M. D., & Zuidema, P. (2005). A new double-moment microphysics parameterization for application in cloud and climate models. Part II: Single-column modeling of arctic clouds. *Journal of the Atmospheric Sciences*, *62*, 1678–1693. <https://doi.org/10.1175/JAS3447.1>
- Pleim, J. E. (2006). A simple, efficient solution of flux–profile relationships in the atmospheric surface layer. *Journal of Applied Meteorology and Climatology*, *45*(2), 341–347. <https://doi.org/10.1175/JAM2339.1>
- Pleim, J. E. (2007). A combined local and nonlocal closure model for the atmospheric boundary layer. Part I: Model description and testing. *Journal of Applied Meteorology and Climatology*, *46*(9), 1383–1395. <https://doi.org/10.1175/JAM2539.1>
- Pleim, J. E., & Xiu, A. (1995). Development and testing of a surface flux and planetary boundary layer model for application in mesoscale models. *Journal of Applied Meteorology*, *34*, 16–32. <https://doi.org/10.1175/1520-0450-34.1.16>
- Qian, T., Zhao, P., Zhang, F., & Bao, X. (2015). Rainy-season precipitation over the Sichuan basin and adjacent regions in southwestern China. *Monthly Weather Review*, *143*(1), 383–394. <https://doi.org/10.1175/mwr-d-13-00158.1>
- Shapiro, A., Fedorovich, E., & Rahimi, S. (2016). A unified theory for the Great Plains nocturnal low-level jet. *Journal of the Atmospheric Sciences*, *73*(8), 3037–3057. <https://doi.org/10.1175/jas-d-15-0307.1>
- Shen, P., & Zhang, Y. (2011). The simulation of the precipitation diurnal variation of Sichuan [in Chinese]. *Plateau Meteorology*, *30*(4), 860–868.
- Skamarock, W. C., Klemp, J. B., Dudhia, J., Gill, D. O., Barker, D. M., Wang, W., & Powers, J. D. (2005). A description of the advanced research WRF version 2Rep., 88 pp, NCAR.
- Steiner, M., Houze, R. A., & Yuter, S. E. (1995). Climatological characterization of three-dimensional storm structure from operational radar and rain gauge data. *Journal of Applied Meteorology*, *34*(9), 1978–2007. [https://doi.org/10.1175/1520-0450\(1995\)034<1978:ccotds>2.0.co;2](https://doi.org/10.1175/1520-0450(1995)034<1978:ccotds>2.0.co;2)
- Sun, J., & Zhang, F. (2012). Impacts of mountain–plains solenoid on diurnal variations of rainfalls along the Mei-Yu front over the East China Plains. *Monthly Weather Review*, *140*(2), 379–397. <https://doi.org/10.1175/mwr-d-11-00041.1>
- Trier, S. B., Davis, C. A., & Carbone, R. E. (2014). Mechanisms governing the persistence and diurnal cycle of a heavy rainfall corridor. *Journal of the Atmospheric Sciences*, *71*(11), 4102–4126. <https://doi.org/10.1175/JAS-D-14-0134.1>
- Wallace, J. M. (1975). Diurnal variations in precipitation and thunderstorm frequency over the conterminous United States. *Monthly Weather Review*, *103*, 406–419. [https://doi.org/10.1175/1520-0493\(1975\)103<0406:DVIPAT>2.0.CO;2](https://doi.org/10.1175/1520-0493(1975)103<0406:DVIPAT>2.0.CO;2)

- Xu, W., & Zipser, E. (2011). Diurnal variations of precipitation, deep convection, and lightning over and east of the eastern Tibetan Plateau. *Journal of Climate*, *24*, 448–465. <https://doi.org/10.1175/2010JCLI3719.1>
- Xue, M., Luo, X., Zhu, K., Sun, Z., & Fei, J. (2018). The controlling role of boundary layer inertial oscillations in Meiyu frontal precipitation and its diurnal cycles over China. *Journal of Geophysical Research: Atmospheres*, *123*, 5090–5115. <https://doi.org/10.1029/2018jd028368>
- Yin, S., Chen, D., & Xie, Y. (2009). Diurnal variations of precipitation during the warm season over China. *International Journal of Climatology*, *29*(8), 1154–1170. <https://doi.org/10.1002/joc.1758>
- Yu, R., Xu, Y., Zhou, T., & Li, J. (2007). Relation between rainfall duration and diurnal variation in the warm season precipitation over central eastern China. *Geophysical Research Letters*, *34*, L13703. <https://doi.org/10.1029/2007GL030315>
- Yu, R., Yuan, W., Li, J., & Fu, Y. (2009). Diurnal phase of late-night against late-afternoon of stratiform and convective precipitation in summer southern contiguous China. *Climate Dynamics*, *35*(4), 567–576. <https://doi.org/10.1007/s00382-009-0568-x>
- Yu, R., Zhou, T., Xiong, A., Zhu, Y., & Li, J. (2007). Diurnal variations of summer precipitation over contiguous China. *Geophysical Research Letters*, *34*, L01704. <https://doi.org/10.1029/2006GL028129>
- Yuan, W. (2013). Diurnal cycles of precipitation over subtropical China in IPCC AR5 AMIP simulations. *Advances in Atmospheric Sciences*, *30*(6), 1679–1694. <https://doi.org/10.1007/s00376-013-2250-9>
- Yuan, W., Yu, R., Zhang, M., Lin, W., Chen, H., & Li, J. (2012). Regimes of diurnal variation of summer rainfall over subtropical East Asia. *Journal of Climate*, *25*(9), 3307–3320. <https://doi.org/10.1175/jcli-d-11-00288.1>
- Zhang, Y.-C., Sun, J.-H., & Fu, S.-M. (2014). Impacts of diurnal variation of mountain-plain solenoid circulations on precipitation and vortices east of the Tibetan Plateau during the Mei-yu season. *Advances in Atmospheric Sciences*, *31*, 139–153.
- Zheng, Y., Xue, M., Chen, J., Li, B., & Tao, Z. (2016). Spatial characteristics of extreme rainfall over China with hourly through 24-hour accumulation periods based on national-level hourly rain gauge data. *Advances in Atmospheric Sciences*, *33*, 1218–1232. <https://doi.org/10.1007/s00376-016-6128-5>
- Zhou, T., Yu, R., Chen, H., Dai, A., & Pan, Y. (2008). Summer precipitation frequency, intensity, and diurnal cycle over China: A comparison of satellite data with rain gauge observations. *Journal of Climate*, *21*(16), 3997–4010. <https://doi.org/10.1175/2008jcli2028.1>
- Zhu, K., & Xue, M. (2016). Evaluation of WRF-based convection-permitting multi-physics ensemble forecasts over China for an extreme rainfall event on 21 July 2012 in Beijing. *Advances in Atmospheric Sciences*, *33*(11), 1240–1258. <https://doi.org/10.1007/s00376-016-6202-z>
- Zhu, K., Xue, M., Zhou, B., Zhao, K., Sun, Z., Fu, P., Zheng, Y., et al. (2018). Evaluation of real-time convection-permitting precipitation forecasts in China during the 2013–2014 summer season. *Journal of Geophysical Research: Atmospheres*, *123*, 1037–1064. <https://doi.org/10.1002/2017JD027445>